**Electronic Supplementary Information (ESI) for**

# Oriented, lightweight and compact graphite-sheet-fin-based solid ammonia carriers enabling risk-free, sustainable onboard ammonia energy supply

Peng Gao[a*], Shikun Fu[a], Baoliang Zhang[a], Kedi Wang[a], Weidong Wu[a], Liwei Wang[b**]
a School of Energy and Power Engineering, University of Shanghai for Science and Technology, Shanghai 200093, China. Email: p.gao@usst.edu.cn
b School of Mechanical Engineering, Shanghai Jiao Tong University, Shanghai, 200240, China. Email: lwwang@sjtu.edu.cn

**Note S1. Theoretical Ammonia Storage Capacity of Metal Chlorides.**

According to Equation 1, each $SrCl_2$ molecule sorbs eight ammonia molecules to form metal ammine [1], $Sr(NH_3)_8Cl_2$, and the seven sorbed ammonia molecules can be completely desorbed at 100°C at 0.2 MPa [2]. The ammonia release amounts for $SrCl_2$ can reach up to 0.75 g/g.

$$\mathrm{Sr(NH_3)8Cl_2\ (Solid)} + 7\Delta H_{\mathrm{r\text{-}Sr(8\text{-}1)}} \leftrightarrow Sr(\mathrm{NH_3})\mathrm{Cl_2}\ (Solid) + 7\mathrm{NH_3(gas)} \quad (1)$$

**Note S2.** $SrCl_2$-reduced graphene oxide (rGO) sorbent

Reference [3] indicates that $SrCl_2$-rGO sorbent with 80 wt% $SrCl_2$ loading demonstrates superior sorption-desorption kinetics. The reference describes the preparation of several small-sized $SrCl_2$-rGO sorbent samples using a bottom-up directional freeze-casting method, with each sample weighing approximately 193 mg and containing 154.4 mg of $SrCl_2$. The dimensions of samples are 20 mm × 20 mm × 20 mm. Further calculations reveal that under sufficient reaction conditions, each sample can sorb 166.86 mg of ammonia gas. Based on these calculations, it is concluded that $SrCl_2$-rGO sorbent with 80 wt% $SrCl_2$ loading theoretically has a volumetric ammonia storage capacity of 20.86 kg/m³.

**Note S3. Preparation process of the graphite-sheet-fin sorbent**

We report a novel strategy of replacing conventional metal fins with graphite-sheet fins, thereby forming a sorbent with lightweight, high ammonia storage density and effective heat and mass transfer performance. Its preparation process is as follows: the graphene oxide dispersion was uniformly mixed with L-ascorbic acid (LAA) and $SrCl_2$ at a specified ratio, transferred into a cylindrical annular Polytetrafluoroethylene mold with a stainless-steel tube in the center, and liquid nitrogen was injected

into the stainless-steel tube to perform low-temperature radial freezing, causing ice crystals to grow radially. After complete radial freezing of the mixture, the sample was freeze-dried and subsequently subjected to high-temperature thermal reduction. The resulting structure can be compressed axially to achieve a tunable packing density as needed (Fig. S1).

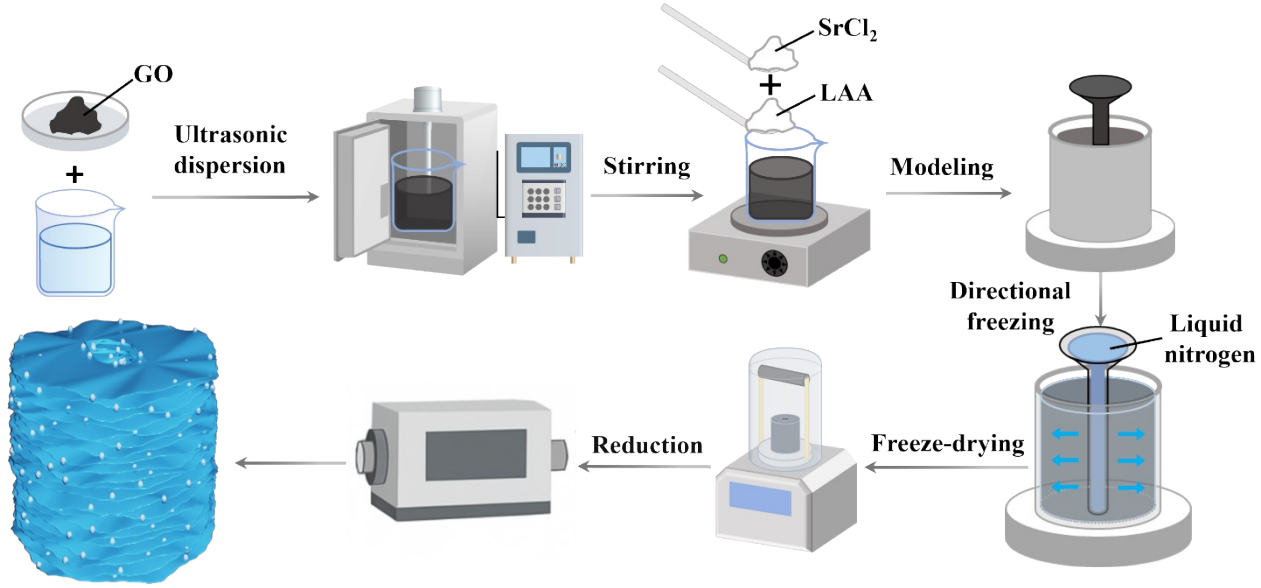


**Fig. S1** Preparation process of the graphite-sheet-fin sorbent

**Note S4. Energy dispersive spectroscopy analysis of graphite-sheet-fin sorbent**

Energy dispersive spectroscopy analysis (Fig. S2) was used to visualize the elemental distribution: Sr (yellow), Cl (blue), and C (red) are homogeneously mixed and distributed throughout the sorbent, demonstrating excellent compositional uniformity.

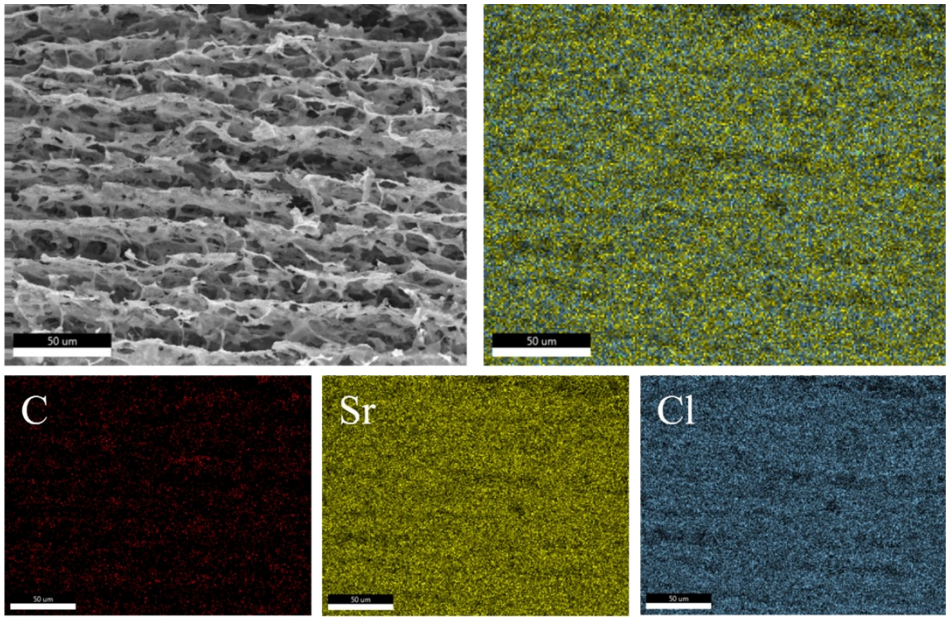


**Fig. S2** Energy dispersive spectroscopy image of graphite-sheet-fin sorbent

**Note S5. Raman, XPS, and XRD characterization of graphite-sheet-fin sorbent**

The Raman spectra (Fig. S3) exhibit characteristic D and G bands at approximately 1350 and 1590 $cm^{-1}$, respectively, indicating that the samples retain a graphitized framework dominated by $sp^2$-hybridized carbon. The $I_D/I_G$values of graphene oxide and the composite are 0.82 and 0.78, respectively. The decrease in $I_D/I_G$after composite formation indicates a reduced degree of structural disorder and enhanced continuity of the $sp^2$-conjugated network, confirming that part of the oxygen-containing functional groups in graphene oxide was effectively removed during the reduction process.

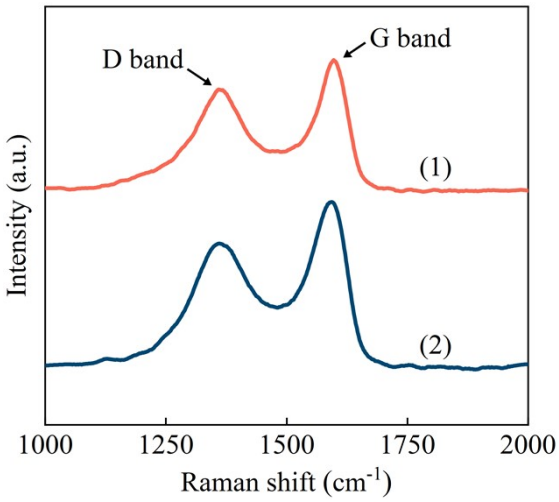


**Fig. S3** Raman spectra: (1) graphite-sheet-fin sorbent; (2) graphene oxide

The XPS spectra (Fig. S4) provide further direct evidence for the surface chemical composition. In the composite sample, the characteristic signals of O 1s, C 1s, Cl 2p, and Sr 3d are simultaneously detected, confirming the coexistence of the carbon framework and $SrCl_2$ within the same sample. In particular, the weak feature located at approximately 270 ~ 280 eV on the right side of the C 1s peak can be assigned to the overlapping Sr 3p and Cl 2s signals. Together with the Cl 2p and Sr 3d peaks, this result further confirms the successful incorporation of $SrCl_2$ into the carbon framework. Meanwhile, the relatively weakened O 1s signal and the prominent C 1s signal in the composite further indicate a reduced content of oxygen-containing groups and an increased C/O ratio in the graphene framework.

The XRD results (Fig. S5) show that the main diffraction peaks of the sample agree well with the standard diffraction pattern of hydrated $SrCl_2$, demonstrating that $SrCl_2$ retains a well-defined crystalline structure after compositing. In addition, no extra diffraction peaks assignable to impurity phases are observed, indicating that no new crystalline by-products were generated during the composite preparation process.

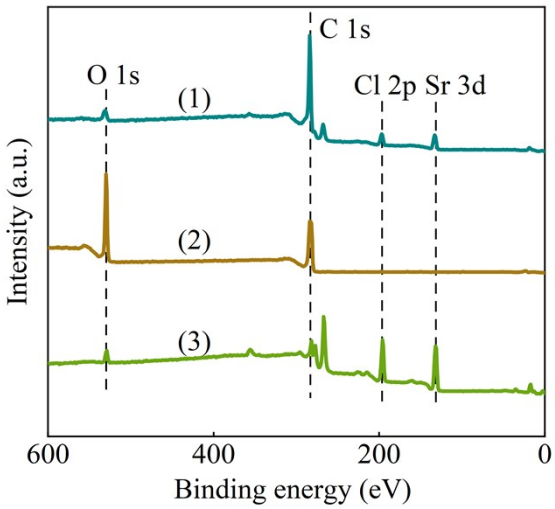


**Fig. S4** XPS spectra: (1) graphite-sheet-fin sorbent; (2) graphene oxide; (3) $SrCl_2$

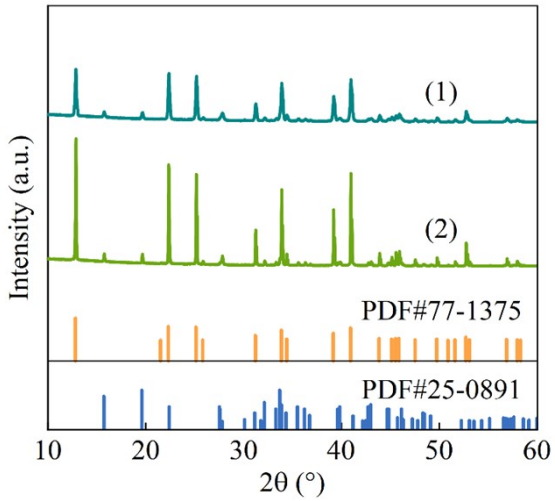


**Fig. S5** XRD patterns: (1) graphite-sheet-fin sorbent; (2) $SrCl_2$

**Note S6. BET of graphite-sheet-fin sorbent**

BET analysis revealed that the graphite-sheet-fin sorbent possesses a specific surface area of 20.8 $m^2/g$. As shown in Fig. S6, the pore size distribution is primarily concentrated between 2 and 50 nm, indicating a mesoporous structure. The average pore diameter was calculated to be 8.8 nm, which is sufficiently large to allow ammonia molecules to diffuse easily to the active sites, thereby enhancing the sorption performance. The adsorption-desorption isotherm exhibits an H3-type hysteresis loop, characteristic of slit-like or wedge-shaped mesopores.

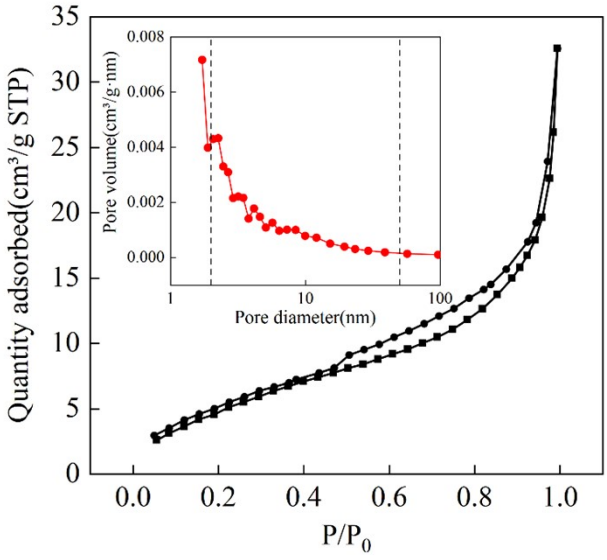


**Fig. S6** BET sorption isotherm of the graphite-sheet-fin sorbent

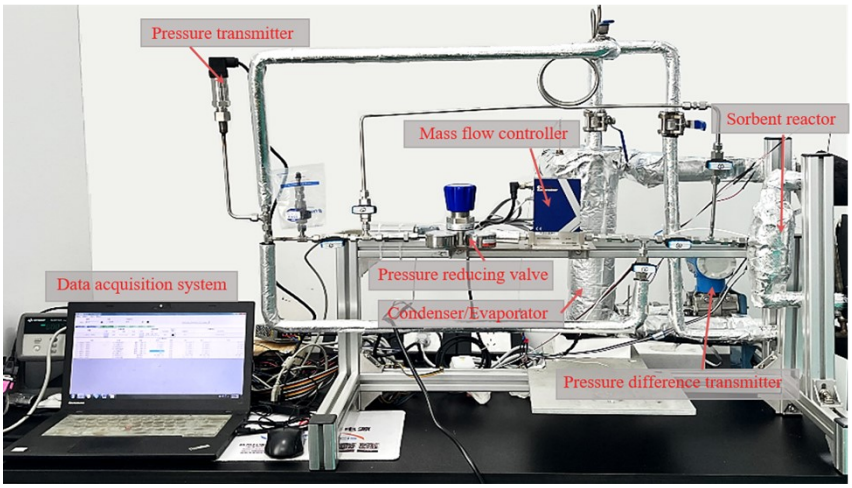


**Fig. S7** Experimental apparatus for ammonia charging and discharging tests of the graphite-sheet-fin sorbent

**Note S7. Ammonia charging and discharging experimental processes**

Due to the maximum inlet pressure limit of the mass flow controller (MFC) and its strictly unidirectional flow characteristics, a pressure reducing valve and a check valve were installed upstream and downstream of the MFC, respectively, to control the maximum system pressure and prevent gas backflow. Prior to high-pressure charging experiments, all valves were closed. Thermostat 1 was set to 20°C, 10°C, or 0°C, and Thermostat 2 was set to 30°C. Once both thermostats reached stable temperatures and the pressure in the evaporator/condenser and the storage unit tube stabilized, valves V1 and V5 remained closed while V3 and V4 were sequentially opened, allowing ammonia gas to flow directly into the unit tube. This configuration simulates the rapid ammonia charging process during the replacement of a solid ammonia storage module. Before conducting desorption experiments, all valves were again closed. Thermostat 1 was set to -20 °C, and Thermostat 2 was set to either 90 °C or 80 °C.

The MFC was configured to flow rates of 190 sccm, 145 sccm, or 100 sccm. After both temperature and pressure conditions stabilized, valves V1 and V4 were kept closed. Valves V5, V2, V3, and the pressure-reducing valve were then sequentially opened, allowing ammonia gas desorbed from the unit tube to first pass through the MFC and then enter the condenser. The MFC flow rate was used to simulate a controlled, quantitative ammonia release process, mimicking actual solid ammonia storage system operation.

**Note S8. Microstructure comparisons of graphite-sheet-fin and $SrCl_2$/ENG sorbents**

SEM image (Fig. S8 and S9) clearly reveals the distinct microstructural differences between the two sorbents. The graphite-sheet-fin sorbent exhibits an ordered, layered morphology with well-defined interlayer spacing. In contrast, the $SrCl_2$/ENG sorbent displays an overall loose architecture, accompanied by severe agglomeration of $SrCl_2$ particles and evident pore blockage. These structural defects in the latter are likely detrimental to heat transfer and the uniformity of gas diffusion pathways during the reaction process, thereby constraining the depth of the sorption/desorption cycles.

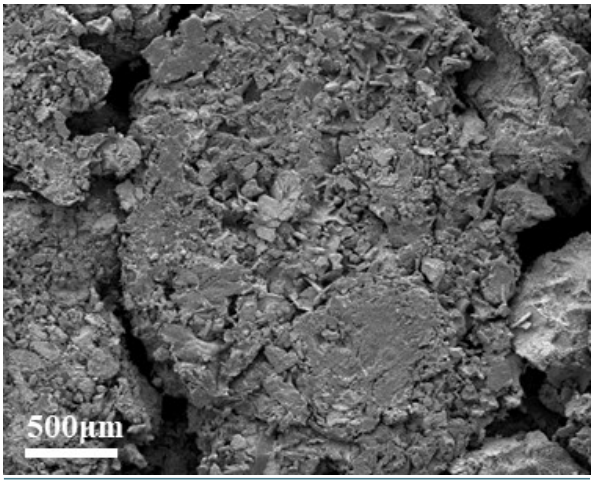


**Fig. S8** SEM image of the $SrCl_2$@ENG sorbent prepared by the oven-drying method

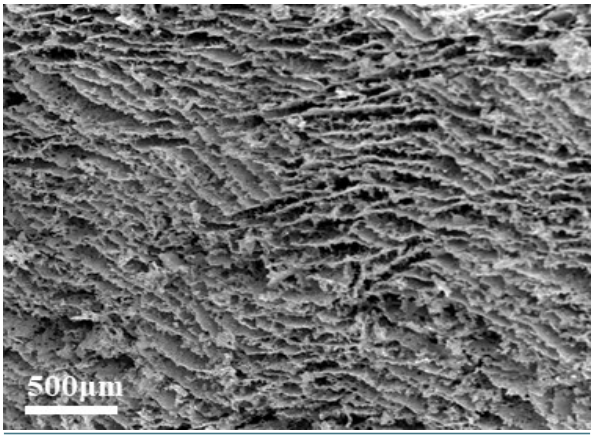


**Fig. S9** SEM image of our graphite-sheet-fin sorbent

**Note S9. Cycling performance of graphite-sheet-fin sorbent.**

A total of 40 operating conditions were defined for the graphite-sheet-fin sorbent, and each condition was tested in 2 ~ 3 repeated runs, resulting in approximately 100 sorption/desorption cycle tests in total. Representative operating conditions are listed as follows. High-pressure sorption conditions included: unit tube at 30°C/evaporator at 20°C, and unit tube at 30°C/evaporator at 10°C. Low-pressure desorption conditions included: unit tube at 90°C/condenser at -20°C/MFC 190 sccm, unit tube at 90°C/condenser at -20°C/MFC 145 sccm, unit tube at 90°C/condenser at -20°C/MFC 100 sccm, unit tube at 80°C/condenser at -20°C/MFC 190 sccm, unit tube at 80°C/condenser at -20°C/MFC 145 sccm, and unit tube at 80°C/condenser at -20°C/MFC 100 sccm.

Among these, the results of two sorption/desorption cycle tests conducted under the individual operating conditions of unit tube at 90°C/condenser at -20°C/MFC 190 sccm and unit tube at 90°C/condenser at -20°C/MFC 145 sccm are shown in Fig. S10. The real-time desorption and sorption curves were found to be nearly identical in the repeated tests. The final experimental results demonstrate that, even after more than one hundred sorption/desorption cycles, the graphite-sheet-fin sorbent still maintained favorable sorption/desorption performance.

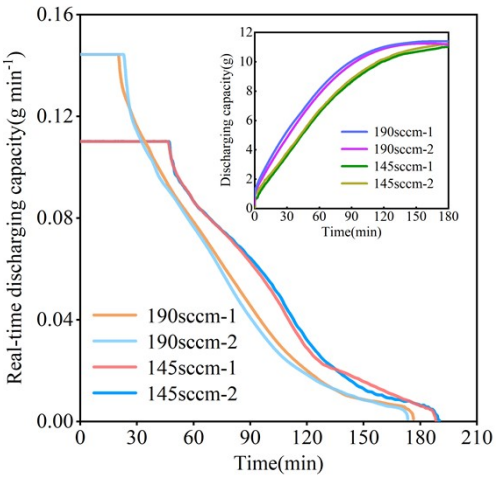


**Fig. S10** Result of two sorption/desorption cycle tests

**Note S10. Conventional metal fins packed with sorbent.**

Reference [4] describes a metal-finned unit tube (Fig. S11), incorporates fins with a pitch of 5 mm, a thickness of 0.4 mm, and a height of 9.5 mm. $SrCl_2$/ENG sorbent is packed into the inter-fin spaces. Based on these structural parameters, only 89.4% of the volume is available for sorbent filling, with the remaining 10.6% occupied by the metal fins. This structural design reduces the sorbent mass that can be loaded into the reactor, and assuming a constant packing density, leads to a corresponding reduction in volumetric ammonia storage density, yielding a maximum of 171.1 kg $m^{-3}$.

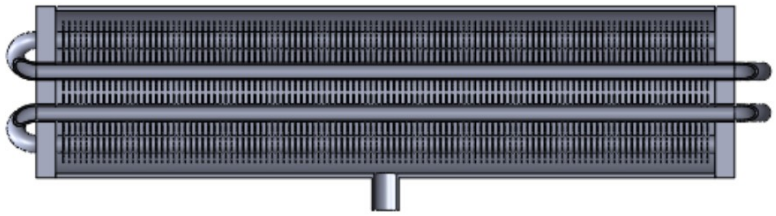

**Fig. S11** Structure of the conventional metal-fin unit tube

**Note S11. Emission of nitrogen oxides ($NO_x$) in transport sector**

The substantial emission of nitrogen oxides ($NO_x$) poses a significant challenge to the global environment and climate [5], and presents a serious threat to human health [6]. $NO_x$ can cause profound damage to the human respiratory system, cardiovascular system, and other physiological functions [7]. Long-term exposure to high concentrations of $NO_x$ also lead to the onset and exacerbation of chronic diseases [8]. Therefore, $NO_x$ treatment has become a pressing major issue in global environmental governance and public health. Exhaust emissions from heavy-duty diesel trucks and cargo ships are one of the most prominent sources of $NO_x$. With the development of the global economy and the growing demand for long-distance logistics, heavy-duty trucks and cargo ships still occupy an important position in the global transportation system, resulting in continuously increasing $NO_x$ emissions [9, 10].

**Note S12. Calculation of Fuel Consumption and Carbon Emission Reduction**

The formulas for calculating the fuel consumption ($FC$) of an ammonia-diesel dual-fuel truck and the fuel consumption ($FC^{'}$) of a conventional diesel truck are:

$$FC = \frac{s}{V_{Diesel}} \#(1)$$

$$FC^{'} = \frac{s}{V_{Diesel}^{'}} \#(2)$$

Where $s$ represents the driving distance of the truck; $V_{Diesel}$ is the volume of diesel consumed by the ammonia-diesel dual-fuel truck over distance $s$; and $V_{Diesel}^{'}$ is the volume of diesel consumed by a conventional truck over the same distance $s$.

Neglecting variations in the engine indicated efficiency, the following energy balance relationship holds for both the conventional truck and the ammonia-diesel dual-fuel truck traveling a distance of $s$:

$$\rho_{Diesel} \times V'_{Diesel} \times LHV_{Diesel} = \rho_{NH_3} \times V_{NH_3} \times LHV_{NH_3} + \rho_{Diesel} \times V_{Diesel} \times LHV_{Diesel} \#(3)$$

Where $\rho_{Diesel}$ is the density of diesel; $\rho_{NH_3}$ is the density of ammonia; $LHV_{Diesel}$ is the lower heating

value of diesel; and $LHV_{NH_3}$ is the lower heating value of ammonia.

The ammonia energy ratio ($AER$) is defined as:

$$AER = \frac{\rho_{NH_3} \times V_{NH_3} \times LHV_{NH_3}}{\rho_{NH_3} \times V_{NH_3} \times LHV_{NH_3} + \rho_{Diesel} \times V_{Diesel} \times LHV_{Diesel}} \#(4)$$

The diesel savings per truck ($\Delta V$) are calculated as:

$$\Delta V = V_{Diesel}^{'} - V_{Diesel} \#(5)$$

The carbon emission reduction for an ammonia-diesel dual-fuel truck ($C_{decrease}$) is:

$$C_{decrease} = f_{CO_2} \times \Delta V \#(6)$$

Where $f_{CO_2}$ represents the mass of $CO_2$ emitted per liter of diesel upon complete combustion.

The total annual carbon emission reduction for $n$ trucks ($C_{decrease,total}$) is:

$$C_{decrease,total} = n \times 365 \times C_{decrease} \#(7)$$

Using the parameters $FC^{'} = 40$ L/100 km; $s = 200$ km; $AER = 0.3$[11]; $f_{CO_2} = 2.63$ kg/L; and $n = 4{,}000$, the results are calculated as follows: $FC = 28$ L/100km; $\Delta V = 24$ L; $C_{decrease} = 63.12$ kg; and $C_{decrease,total} = 92{,}155$ t.

**Note S13. Calculation of NOx Treatment**

In the Selective Catalytic Reduction (SCR) system of a conventional diesel truck, the urea solution consumption ($UC^{'}$) accounts for 5% to 8% of the diesel fuel consumption ($FC^{'}$). This relationship is expressed as:

$$5\% \leq \frac{UC^{'}}{FC^{'}} \leq 8\% \#(8)$$

The volume of diesel that can be treated per liter of urea solution ($V_{treat,v}$) is defined as:

$$V_{treat,v} = \frac{FC^{'}}{UC^{'}} \#(9)$$

Consequently, the volume of diesel that can be treated per kilogram of ammonia ($V_{treat,m}$) is calculated by:

$$V_{treat,m} = \frac{V_{treat,v}}{\rho_{NH_3,urea}} \#(10)$$

Where $\rho_{NH_3,urea}$ represents the mass of ammonia per unit volume of urea solution (32.5 wt%).

For an ammonia-diesel dual-fuel truck, the ammonia stored in a graphite-sheet-fin sorbent with volume $V$ can treat the $NO_x$ generated during a driving distance $d$. The formula for calculating $d$ is:

$$d = \frac{\rho_{NH_3,sorbent} \times V \times V_{treat,m}}{FC} \#(11)$$

Where $\rho_{NH_3,sorbent}$ denotes the mass of ammonia stored per unit volume of the graphite-sheet-fin sorbent.

In a conventional diesel truck, the ammonia stored in a urea solution volume $V$ can treat the $NO_x$ generated during a driving distance $d'$. The formula for calculating $d'$ is:

$$d' = \frac{\rho_{NH_3,urea} \times V \times V_{treat,m}}{FC'} \#(12)$$

Using the parameters $\rho_{NH_3,urea} = 200\ \text{kg m}^{-3}$; $V = 18\ \text{L}$; and the experimentally measured $\rho_{NH_3,sorbent} = 216.9\ \text{kg m}^{-3}$, the results are calculated as: $562\ \text{km} \leq d' \leq 900\ \text{km}$ and $871\ \text{km} \leq d \leq 1394\ \text{km}$. The endurance mileage of the $NO_x$ treatment system is increased by 55%.

**Note S14. Fabrication of solid ammonia storage unit tube employing graphite-sheet-fin sorbent**

A custom-designed mold was used to tailor the shape of the sorbent blocks **(**Fig. S12**)**. A funnel was connected to the stainless-steel tube embedded in the mold via flexible tubing, allowing liquid nitrogen to be injected into the tube. This setup enabled radial freezing of the sample from the center outward via the stainless-steel tube. The mold was designed for batch processing, allowing multiple samples to be frozen simultaneously. After freeze-drying, the fully dried samples were demolded using a specialized tool, thermally reduced in a tubular furnace, and then compressed using a custom pressing device. Multiple sorbent blocks were stacked in series and encapsulated within a porous mesh tube to form the final solid ammonia storage unit.

**Note S15. Fabrication of solid ammonia storage unit tube employing SrCl2@ENG sorbent**

To systematically evaluate the performance advantages of the graphite-sheet-fin sorbent, an equivalent mass and proportion of $SrCl_2$/ENG sorbent was prepared according to the procedure reported in Reference [12], as illustrated in Fig. S13. The sorbent was synthesized as follows: $SrCl_2$ and ENG-TSA were added to deionized water. The mixture was then subjected to magnetic stirring and ultrasonic dispersion to form a homogeneous suspension, which was subsequently dried in an oven to obtain the final $SrCl_2$@ENG sorbent.

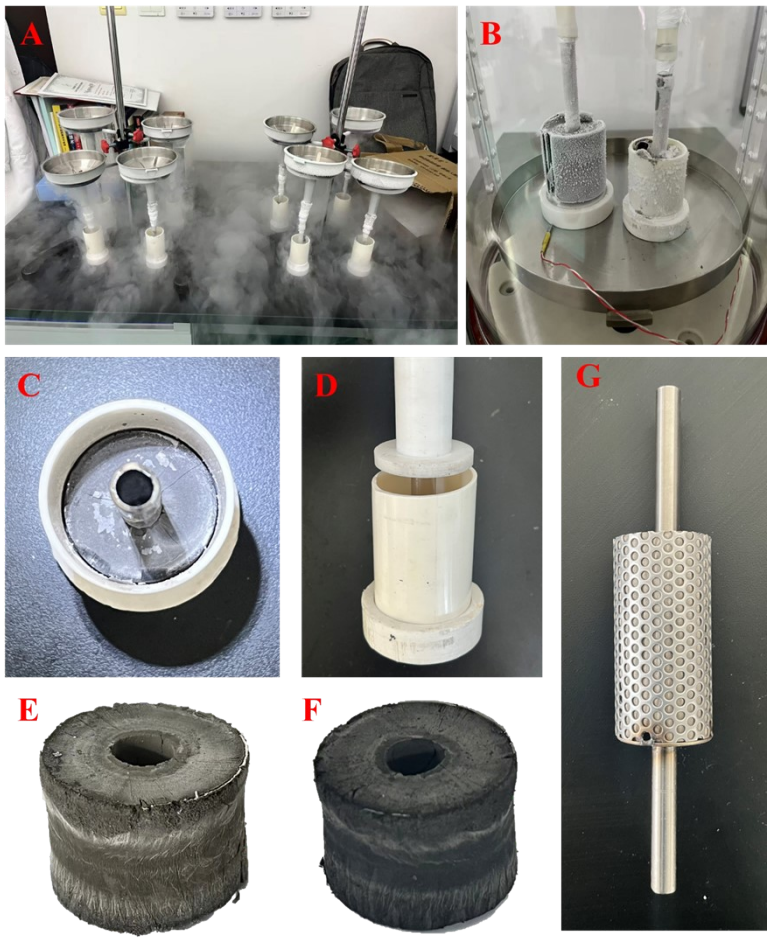


**Fig. S12** Fabrication process of the solid ammonia carriers: (a) multiple samples undergoing simultaneous freezing; (b) samples during the freeze-drying process; (c) fully dried samples; (d) custom tools used for demolding and compression; (e) demolded samples; (f) samples after thermal reduction in a tubular furnace; (g) final solid ammonia storage unit tube after porous mesh tube encapsulation.

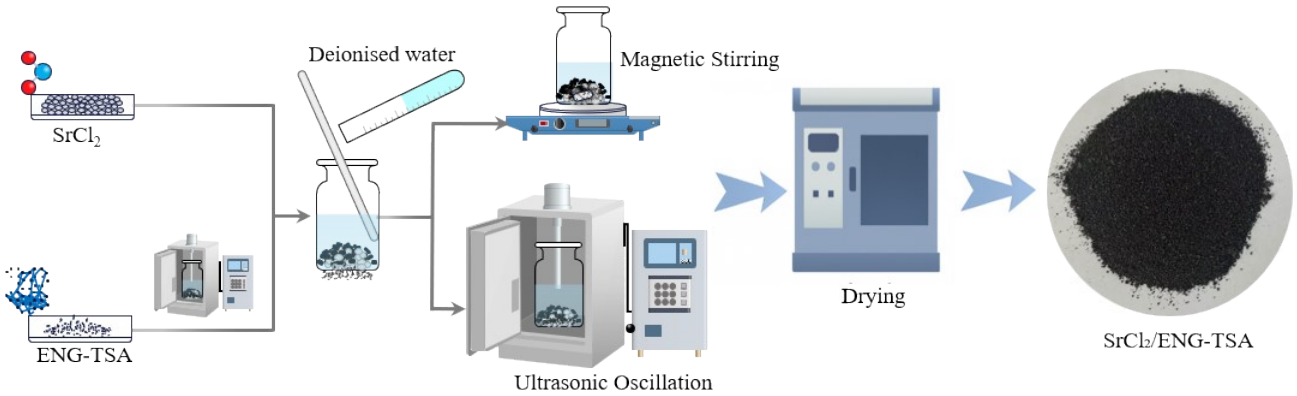


**Fig. S13** Synthesis procedure of the $SrCl_2$@ENG sorbent

## References


1. G. L. An, L. W. Wang, J. Gao and R. Z. Wang, *Renewable and Sustainable Energy Reviews*, 2018, **91**, 783-792.

2. L. W. Wang, R. Z. Wang and R. G. Oliveira, *Renewable & Sustainable Energy Reviews*, 2009, **13**, 518-534.

3. Z. Cao and F. Akhtar, *Advanced Functional Materials*, 2021, **31**, 2008505.

4. T. Yan, R. Z. Wang and T. X. Li, *Energy*, 2018, **143**, 562-574.

5. J. Vazquez Santiago, H. Hata, E. J. Martinez-Noriega and K. Inoue, *Nature Communications*, 2024, **15**, 10236.

6. W. Huang, H. Xu, J. Wu, M. Ren, Y. Ke and J. Qiao, *Science*, 2024, **385**, 386-390.

7. Ł. Kuźma, E. J. Dąbrowski, A. Kurasz, M. Święczkowski, P. Jemielita, M. Kowalewski, W. Wańha, P. Kralisz, A. Tomaszuk-Kazberuk, H. Bachórzewska-Gajewska, S. Dobrzycki and G. Y. H. Lip, *The Lancet Regional Health – Europe*, 2024, **41**.

8. X. Xia, C. Liu, Y. Niu, X. Meng, N. Wright, C. Kartsonaki, Y. Chen, L. Yang, H. Du, C. Yu, D. Sun, J. Lv, J. Chen, L. Li, M. Barnard, K. Kang, S. Wu, K. H. Chan, K. B. H. Lam, H. Kan and Z. Chen, *The Lancet Regional Health – Western Pacific*, 2025, **62**.

9. X. Xu, X. Zhang, Y. Zou, T. Chen, J. Zhan, L. Cheng, W. Winiwarter, S. Zhang, P. M. Vitousek, W. de Vries and B. Gu, *Science*, 2025, **388**, 1098-1103.

10. Y. Zhang, J. Du, Y. Shan, F. Wang, J. Liu, M. Wang, Z. Liu, Y. Yan, G. Xu, G. He, X. Shi, Z. Lian, Y. Yu, W. Shan and H. He, *Chemical Society Reviews*, 2025, **54**, 1151-1215.

11. Z. Jin, S. Mi, D. Zhou, J. Zhu, A. Schirru, W. Zhao, Y. Qian, T. Lucchini and X. Lu, *Applied Energy*, 2024, **373**, 123894.

12. P. Gao, H. Hu, S. Jin, S. Wang, Y. Chen, W. Wu, Q. Yang, F. Zhu and L. Wang, *Energy Conversion and Management*, 2022, **258**, 115474.